The Astrophysical Journal, 1002:106 (14pp), 2026 May 1 https://doi.org/10.3847/1538-4357/ae581d

Resolved UV–Optical HST Imaging and Spectral Energy Distribution Modeling of Nearby BAT Active Galactic Nuclei

Connor Auge[1], Michael Koss[1], Kriti K. Gupta[2,3], Claudio Ricci[4,5], Benny Trakhtenbrot[6], Franz E. Bauer[7], Ezequiel Treister[7], Alessandro Peca[1,8], Brad Cenko[9], Kohei Ichikawa[10], Arghajit Jana[11], Darshan Kakkad[12], Richard Mushotzky[13], Kyuseok Oh[14], Alejandra Rojas Lilayú[15], David Sanders[16], Roberto Serafinelli[4,17], Matilde Signorini[18,19], Alessia Tortosa[17], and C. Megan Urry[20]
[1] Eureka Scientific, Inc., 2452 Delmer Street, Suite 100, Oakland, CA 94602-3017, USA; connor.auge@gmail.com
[2] STAR Institute, Liège Université, Quartier Agora—Allée du six Août 19c, B-4000 Liège, Belgium
[3] Sterrenkundig Observatorium, Universiteit Gent, Krijgslaan 281 S9, B-9000 Gent, Belgium
[4] Instituto de Estudios Astrofísicos, Facultad de Ingeniería y Ciencias, Universidad Diego Portales, Avenida Ejército Libertador 441, Santiago, Chile
[5] Kavli Institute for Astronomy and Astrophysics, Peking University, Beijing 100871, People's Republic of China
[6] School of Physics and Astronomy, Tel Aviv University, Tel Aviv 69978, Israel
[7] Instituto de Alta Investigación, Universidad de Tarapacá, Casilla 7D, Arica, Chile
[8] Department of Physics, Yale University, P.O. Box 208120, New Haven, CT 06520, USA
[9] Astrophysics Science Division, NASA Goddard Space Flight Center, Mail Code 661, Greenbelt, MD 20771, USA
[10] Frontier Research Institute for Interdisciplinary Sciences, Tohoku University, Sendai 980-8578, Japan
[11] Department of Physics, SRM University AP, Amaravati 522240, India
[12] Centre for Astrophysics Research, University of Hertfordshire, College Lane, Hatfield, AL10 9AB, UK
[13] Department of Astronomy, University of Maryland, College Park, MD 20742, USA
[14] Korea Astronomy and Space Science Institute, Daedeokdae-ro 776, Yuseong-gu, Daejeon 34055, Republic of Korea
[15] Departamento de Física, Universidad Técnica Federico Santa María, Vicuña Mackenna 3939, San Joaquín, Santiago, Chile
[16] Institute for Astronomy, University of Hawai'i, 2680 Woodlawn Drive, Honolulu, HI 96822, USA
[17] INAF—Osservatorio Astronomico di Roma, Via Frascati 33, 00078, Monte Porzio Catone (Roma), Italy
[18] European Space Agency (ESA), European Space Research and Technology Centre (ESTEC), Keplerlaan 1, 2201 AZ Noordwijk, The Netherlands
[19] INAF—Osservatorio Astrofisico di Arcetri, Largo Enrico Fermi 5, I-50125 Firenze, Italy
[20] Physics Department and Yale Center for Astronomy & Astrophysics, Yale University, New Haven, CT 06520, USA
Received 2025 November 25; revised 2026 March 2; accepted 2026 March 22; published 2026 April 29

Abstract

We use high-resolution UV-to-optical imaging from the Hubble Space Telescope (HST) to construct spatially resolved spectral energy distributions (SEDs) for seven nearby ($z < 0.07$) hard (14–195 keV) X-ray-selected broad-line active galactic nuclei (AGN) with $L_{\rm bol} = 10^{43.26}$–$10^{45.34}$ erg s^{-1}. The high spatial resolution of HST, which physically resolves structures on the scale of ∼50 pc at $z = 0.05$, enables the separation of AGN and host-galaxy emission through morphological decomposition with GALFIT, yielding improved measurements of AGN properties compared to those obtained with lower-resolution Swift UV/Optical Telescope (UVOT) data. AGN UV magnitudes derived from HST imaging (e.g., F225W) can differ by more than a magnitude from those from Swift/UVOT UVM2 due to extended nuclear emission. Additionally, the inclusion of high-resolution data at longer wavelengths (e.g., F814W) can significantly affect the resulting SED fit. Comparing fits of accretion disk and extinction models using HST and Swift/UVOT data, we find significant differences in the resulting parameters, with average differences of 2.0 eV in the maximum disk temperature and 2.2 mag in the AGN host-galaxy extinction. These differences ultimately lead to significant changes in bolometric luminosities and X-ray bolometric corrections, with the HST-based fits yielding average increases of ∼0.57 dex and ∼0.66 dex, respectively. This demonstrates host-galaxy contamination in unresolved UV–optical data can strongly bias SED-based estimates of disk temperatures, extinction, bolometric luminosities, and X-ray bolometric corrections in AGN. Large-area, high-resolution imaging surveys from Euclid and the Nancy Grace Roman Space Telescope will extend these techniques to much larger AGN samples, enabling uniform, high-precision SED measurements in the near-IR.

Unified Astronomy Thesaurus concepts: AGN host galaxies (2017); Spectral energy distribution (2129); HST photometry (756); X-ray active galactic nuclei (2035); Active galactic nuclei (16)

1. Introduction

Active galactic nuclei (AGN) produce intense multiwavelength emission (X-ray to radio) through various physical processes. The accretion disk directly produces UV-to-optical emission, while X-rays are produced via inverse Compton scattering of UV photons in the X-ray corona. Near-IR (NIR) to far-IR emission is generated via the reprocessing of shorter-wavelength emission by dust at varying distances from the supermassive black hole (SMBH; see H. Netzer 2015; R. C. Hickox & D. M. Alexander 2018 for reviews). These multiwavelength observables are dependent on the level of obscuration surrounding the central engine, which may be driven by the SMBH accretion properties (C. Ricci et al. 2017a), or by dust located relatively near the accretion disk (∼10–100 pc; M. Kishimoto et al. 2011; S. F. Hönig 2019; A. Alonso-Herrero et al. 2021) or at larger distances from the

galactic nucleus within the host galaxy (A. D. Goulding et al. 2012; R. Gilli et al. 2022; B. Vijarnwannaluk et al. 2024).

While detailed broadband spectral energy distributions (SEDs) can provide unique insights into these emission processes, and thus into the intrinsic properties of the physical mechanisms driving them, accurately disentangling the AGN emission from that of the host galaxy can be exceedingly challenging. Host-galaxy contamination is particularly important in low-luminosity AGN and/or heavily obscured AGN, where the UV–optical emission from stars can dominate over that of the AGN (e.g., L. C. Ho 2008; B. D. Simmons et al. 2011; A. Peca et al. 2021).

SED-fitting software, such as CIGALE (M. Boquien et al. 2019; G. Yang et al. 2022), AGNfitter (G. Calistro Rivera et al. 2016), AGNFITTER-RX (L. N. Martínez-Ramírez et al. 2024), and SED3FIT (S. Berta et al. 2013), models the combined emission and disentangles the emission from the AGN and host-galaxy components through statistical means or by utilizing the AGN X-ray emission (G. Yang et al. 2020). However, with the use of high-resolution imaging data and tools such as GALFIT (C. Y. Peng et al. 2002), the host-galaxy light can be effectively removed from the SED before any fitting is conducted (e.g., R. V. Vasudevan & A. C. Fabian 2009; Z. Shang et al. 2011).

The BAT AGN Spectroscopic Survey (BASS; M. Koss et al. 2017)[21] contains 858 nearby hard X-ray-selected AGN, detected using the 14–195 keV band of the Burst Alert Telescope (BAT) on board NASA's Neil Gehrels Swift Observatory (N. Gehrels et al. 2004). The BASS sample was selected from the 70 month catalog (W. H. Baumgartner et al. 2013); see also the 105 month (K. Oh et al. 2018) and 157 month catalogs (A. Y. Lien et al. 2025). The Swift-BAT survey selects the nearest and brightest hard X-ray-selected AGN in the sky, with its all-sky coverage up to Compton-thick ($N_{\rm H} = 10^{24}\,{\rm cm}^2$) obscuration levels (M. J. Koss et al. 2016).

Most of the sources observed by BAT in the hard X-ray band have also been observed in the soft X-ray (0.5–10 keV) band with the X-ray Telescope (XRT; D. N. Burrows et al. 2005; J. E. Hill et al. 2005) and with the UV/Optical Telescope (UVOT; P. W. A. Roming et al. 2005; T. S. Poole et al. 2008; A. A. Breeveld et al. 2010) on Swift. The second data release (DR2) of BASS also compiled a complete optical spectroscopic analysis of all AGN in the 70 month catalog (W. H. Baumgartner et al. 2013), providing an unprecedented collection of multiwavelength data with black hole masses measured for 96% of the sample (M. J. Koss et al. 2022c). Detailed BASS studies have been conducted in the X-ray (C. Ricci et al. 2017b; T. T. Ananna et al. 2022), NIR (M. J. Koss et al. 2018), mid-IR (MIR; K. Ichikawa et al. 2017, 2019; T. T. Shimizu et al. 2017), millimeter (M. J. Koss et al. 2021), and radio (K. L. Smith et al. 2016; T. Kawamuro et al. 2023; M. Magno et al. 2025), providing measurements of both broad and narrow emission lines (K. Oh et al. 2022), velocity dispersions (M. J. Koss et al. 2022a), and NIR spectral properties (J. Gillette et al. 2026).

Recently, K. K. Gupta et al. (2024, hereafter G24) highlighted the power of isolating the AGN emission from that of the host galaxy using GALFIT, fitting Swift/UVOT data with a point source and Sérsic model for a sample of 236 nearby AGN from BASS. The resulting fits yielded the emission from the point-source component for each Swift/UVOT filter (V, B, U, UVW1, UVM2, and UVW2) for each source. Using these data, along with Swift/XRT observations taken simultaneously to minimize variability effects, G24 were able to fit the AGN SED using a variety of phenomenological models, ultimately deriving AGN characteristics such as the disk temperatures and bolometric corrections (κ_λ) for a sample an order of magnitude larger than previously analyzed in this way.

In this work, we expand on the findings presented in G24 and highlight the advantages of using higher-resolution data from the Hubble Space Telescope (HST) to more accurately remove any extended emission in the bulge of the host galaxy that may remain unresolved in the Swift/UVOT data. We compare directly to the results in G24 for seven nearby ($z < 0.07$) hard X-ray-selected AGN, chosen to have the best combination of HST observations currently available for this analysis (see Section 2).

This paper is organized as follows. In Section 2, we describe the photometric data used in this work and the sample selection. Section 3 presents the data analysis, including the process of determining point-source magnitudes using GALFIT for each source and the fitting of the resulting SED AGN disk models. Finally, in Section 4, we compare the SED fits with the results derived from the Swift/UVOT data in G24. We assume a cosmological model with $H_0 = 70\,{\rm km\,s^{-1}\,Mpc^{-1}}$, $\Omega_{\rm M} = 0.3$, and $\Omega_\Lambda = 0.7$ throughout.

2. Data and Sample

More than 506 BAT AGN have optical HST imaging available through a completed 5 yr gap program with the HST Advanced Camera for Surveys (ACS) Wide Field Channel (WFC) in the i band, covering the entire sample at $z < 0.1$ (M. Kim et al. 2021), in addition to an ongoing gap program with g-band observations of 356 AGN and Wide Field Camera 3 (WFC3)/UVIS F225W data from a recent HST SNAP program. In this work, we use data from three SNAP programs: UV 225W (#16241; PI: Koss), 435W (#17310; PI: Koss), and F814W (#15444; PI: Barth). While the Swift/UVOT point-spread functions (PSFs) range from 2″ to 3″ (~0.4–4 kpc for $0.01 < z < 0.05$), comparable to the typical sizes of bulge components in large galaxies, the PSFs of the HST data range between 0.″075 and 0.″08 (~ 20–80 pc for $0.01 < z < 0.05$). The higher resolution of the HST data enables more accurate identification of AGN emission relative to the rest of the host-galaxy bulge, which can be confused in lower-resolution Swift/UVOT data. The improvement in resolution between the HST and Swift/UVOT data is shown in Figure 1. Extended features can be very clearly identified in the two right columns of Figure 1 (NGC7603 and UGC524). These features are within the central 2 kpc of the image and are not resolved in the Swift/UVOT images.

To compare the results of this analysis with those reported in G24, we use the same Swift/UVOT data as in their study. We gather the Swift/UVOT data, along with the corresponding Swift/XRT data, from the HEASARC archive.[22] We selected appropriate data based on the matching observation IDs listed in G24, which were originally selected to provide the best possible estimates of the UV/optical fluxes at the time of that study. While more recent observations are available for

[21] https://www.bass-survey.com/

[22] https://heasarc.gsfc.nasa.gov/cgi-bin/W3Browse/w3browse.pl

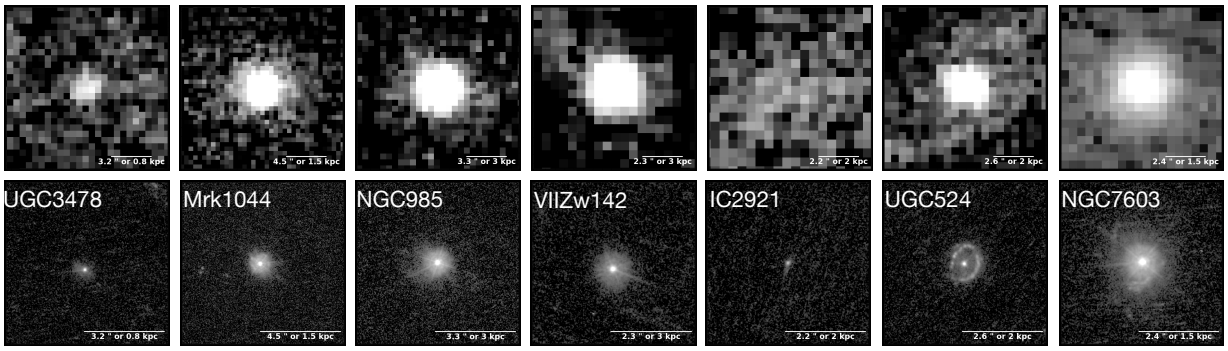

Figure 1. Cutout images of the Swift/UVOT data in the UVM2 band (top) and the HST UVIS data in the F225W band (bottom) for each source in the sample. These two filters have approximately the same central wavelength (2246.43 Å and 2357.65 Å, respectively), and the scale of each image is identical. The increased resolving power of the HST data reveals extended features that are not visible in the Swift/UVOT data. The difference in the UV magnitude of the central point source, as measured from the Swift and HST data, increases from left to right and is listed in Table 2.

Table 1
Sample Properties

BAT ID (1)	Counterpart Name (2)	z (3)	$\log M_{\rm BH}$ (4)	$\log L_{2-10\,\rm keV}$ (5)	$\log L_{\rm bol}$ (6)	$\log \lambda_{\rm Edd}$ (7)	Spectral Type (8)
1189	NGC7603	0.023	8.59	43.62	45.34	−1.95	Sy1
335	UGC3478	0.012	6.06	42.29	43.26	−0.84	Sy1.5
34	UGC524	0.036	7.62	42.71	44.44	−1.49	Sy1.5
134	NGC985	0.043	8.11	43.76	44.98	−1.32	Sy1.5
925	VIIZw142	0.063	7.43	43.15	44.61	−1.07	Sy1.5
130	Mrk1044	0.016	6.45	42.23	44.04	−0.58	Sy1
549	IC 2921	0.043	7.70	42.82	44.29	−1.058	Sy1.5

Note. Column (1): Swift/BAT ID (W. H. Baumgartner et al. 2013). Column (2): counterpart galaxy name. Column (3): spectroscopic redshift (M. J. Koss et al. 2022b). Column (4): SMBH mass in solar masses (J. E. Mejía-Restrepo et al. 2022; M. J. Koss et al. 2022b). Column (5): logarithm of the 2–10 keV X-ray luminosity (erg s^{-1}; C. Ricci et al. 2017b). Column (6): logarithm of the AGN bolometric luminosity from G24 (erg s^{-1}). Column (7): logarithm of the Eddington ratio. Column (8): optical spectral type (K. Oh et al. 2022).

some sources, we chose to utilize the same dataset to enable a more direct comparison with their original work. The potential effects of variability on the analysis are discussed in Section 3.3.

We obtained X-ray data from the Swift/XRT instrument using the UK Swift Science Data Centre online data portal.[23] The downloaded data included cleaned and calibrated event files, automatically extracted source and background spectra, Ancillary Response Files (ARFs), and Response Matrix Files (RMFs), all generated using standard pipeline settings. These spectra are based on default source and background extraction regions optimized for point sources, and are suitable for spectral fitting with XSPEC (K. A. Arnaud 1996). All data correspond to observations taken in photon-counting mode.

We highlight seven BASS AGN in this work to examine how higher-resolution HST data affect the derived AGN properties and to identify which properties are most sensitive to differences in resolution and variability. The sample was selected by identifying all BASS sources that meet the following requirements: one short (5–20 s) and one long (>500 s) exposure in the same three HST bands, WFC3 UVIS F225W, ACS/WFC F435W, and ACS/WFC F814W (with central wavelengths of 2371.15 Å, 4329.85 Å, and 8045.53 Å, respectively); a Swift/XRT observation within 4 months of the WFC3 UVIS F225W observation; and inclusion in the G24 analysis. The properties of the seven sources are listed in Table 1 and are taken from the BASS DR2 catalog (M. J. Koss et al. 2022c). These sources span a wide range of black hole masses ($M_{\rm BH}$), Eddington ratios ($\lambda_{\rm Edd} = L_{\rm bol}/L_{\rm Edd}$), and redshifts ($0.01 < z < 0.065$), as shown in Table 1. The HST data presented in this article were obtained from the Mikulski Archive for Space Telescopes at the Space Telescope Science Institute. The specific observations analyzed are available at doi:10.17909/yxsq-td83.

3. Analysis

3.1. Large-aperture Photometry

Large-aperture photometry was first performed on each source using both Swift/UVOT and HST data in the UVM2 and F225W filters, respectively, in order to assess data quality and identify any obvious signs of variability between the Swift/UVOT and HST observations in the UV. The large-aperture photometry of the Swift/UVOT data was carried out following the steps outlined in the Swift/UVOT data-analysis guide,[24] using region files for the source and background defined in SAOImageDS9. These region files, along with the image data, were input into the `uvotsource` command from the Swift calibration database, which returns the flux density and magnitude within a 5″ radius aperture defined for each image. For the HST data, we followed the procedure outlined in the WFC3 data handbook,[25] using the drizzled (DRZ)

[23] https://www.swift.ac.uk/swift_portal/

[24] https://www.Swift.ac.uk/analysis/uvot/mag.php

[25] https://HST-docs.stsci.edu/wfc3dhb/chapter-9-wfc3-data-analysis/9-1-photometry

Table 2
Large-aperture Photometry and GALFIT Point-source Magnitudes

BAT ID	Counterpart	Large Aperture		PSF Magnitudes						
		UVM2	F225W	UVM2	*B*	*V*	F225W	F435W	F814W	F225W – UVM2
(1)	(2)	(3)	(4)	(5)	(6)	(7)	(8)	(9)	(10)	(11)
1189	NGC7603	13.90	15.05	14.44	14.50	13.96	15.50	14.27	13.89	1.06
335	UGC3478	18.93	18.69	19.33	16.94	16.19	19.76	16.72	15.59	0.43
34	UGC524	18.03	18.05	18.36	16.79	16.25	19.66	18.87	18.04	1.30
134	NGC985	15.17	14.98	15.22	15.27	14.87	15.27	15.04	15.00	0.05
925	VIIZw142	17.10	16.85	17.22	16.94	16.44	17.90	16.53	16.99	0.68
130	Mrk1044	15.17	14.98	15.28	15.27	15.43	15.97	15.06	15.09	0.69
549	IC 2921	17.10	16.85	22.15	17.15	16.44	21.82	18.97	16.69	−0.33

Note. Column (1): Swift/BAT ID. Column (2): host-galaxy counterpart name. Column (3): AB magnitude from 5″ aperture photometry of UVOT UVM2. Column (4): AB magnitude from 5″ aperture photometry of HST/UVIS2 F225W. Columns (5)–(7): GALFIT point-source AB magnitudes for UVM2, *B*, and *V* from G24. Columns (8)–(10): GALFIT point-source AB magnitudes for HST F225W, F435W, and F814W. Column (11): the difference between the point-source magnitudes in the F225W and UVM2 filters.

images from the HST data-reduction pipeline. To enable a direct comparison, we adopted a 5″ aperture for both the Swift/UVOT and HST data, which necessarily includes some or all of the bulge of the host galaxy in addition to the AGN point-source emission. These values are reported in the "Large Aperture" photometry columns of Table 2 for the Swift/UVOT UVM2 and HST F225W filters.

Comparing the magnitudes measured within this large aperture allows for a direct comparison between the HST data analyzed in this work and the Swift/UVOT data analyzed in G24, without differences in the morphological decomposition (such as PSF selection) affecting the photometric measurements. When using the same large aperture size, similar levels of contamination from the host-galaxy bulge should be present in each measurement, thus providing a clearer comparison of data quality and providing a check for the presence of variability. Differences in the measurements of the large-aperture photometry should be less sensitive to the increased resolution between the two datasets than measurements that rely on the morphological decomposition discussed in the following section.

3.2. Morphological Decomposition

As previously noted, large-aperture photometry of AGN generally leads to significant levels of contamination from the host galaxy, even for highly luminous and unobscured sources. As shown in Figure 1, the 5″ aperture photometry performed in the previous section includes structures that are likely associated with nuclear star formation in the host galaxy, covering physical scales of ∼0.2–1 kpc at these redshifts. While the level of host-galaxy contamination is difficult to assess in the Swift/UVOT images, extended emission can be clearly identified in each aperture in the higher-resolution HST imaging data.

To obtain more accurate measurements of the AGN flux with as little host-galaxy contamination as possible, we followed the methods outlined by G24. We employed GALFIT (C. Y. Peng et al. 2002) to fit the two-dimensional surface-brightness profiles of the sources and decompose them into AGN and galaxy light. GALFIT is an image-analysis tool that models galaxy light profiles using radial distributions such as PSF, Sérsic, and Gaussian functions to fit the data and separate the components of the sources, including the AGN point source, disk, and bulge. It fits the specified functions to the two-dimensional imaging data and provides best-fit results based on least-squares statistics.

The primary component of the fits performed in this analysis is the PSF function. This requires a PSF image for each fit. For the ACS/WFC3 F435W and F814W filters, we created PSF images for each source using the astropy `photutils` EPSFBuilder (L. Bradley et al. 2025). This method averages bright stars in the source image to create an effective PSF. The stars were selected by visual inspection, with three to five stars chosen per image. Once cutouts were generated for each selected star, a PSF image was created using the `epsf_builder` function.

The WFC3 UVIS F225W images rarely contained a sufficient number of bright stars to construct a suitable PSF using this method. Therefore, an empirical PSF model was utilized for this filter. The PSFs were acquired from the WFC3 instrument page at the Space Telescope Science Institute.[26] They are presented as a grid of 56 fiducial PSFs representing the spatial variation of the PSF across the detector. For each image in this work, the PSF closest to the source on the detector was used in the GALFIT routine. While this approach may be less ideal than constructing a PSF using stars in the science image, since the model PSFs do not show any potential temporal variations that may be present in the PSF, it is the recommended method by the Space Telescope Science Institute when suitable stars are not available.

Each source had both a short and long exposure in each filter. The short exposure times ranged from 5 to 20 s, and the long exposure times ranged from 670 to 1040 s, depending on the filter and source. Fits were performed on both the long and short exposures for each image to assess consistency and estimate the uncertainty in the resulting PSF magnitude. Several of the long-exposure images, particularly those taken in F814W, were saturated at the center of the galaxy. For each of these images, the saturated pixels were masked and replaced with scaled pixels from the short-exposure image after properly aligning the two exposures. The results of the short-exposure fits are used for the remainder of the analysis, as they typically yield better fit statistics (reduced χ^2) and residuals, and are less likely to be affected by saturation. However, the results of the long and short exposures are compared directly to ensure that the derived point-source magnitudes are

[26] https://www.stsci.edu/hst/instrumentation/wfc3/data-analysis/psf

consistent within errors. If inconsistencies are found, the fits are reexamined and repeated, making alterations to the PSFs or fitting parameters as needed until consistent results are achieved.

Each fit includes three components: a PSF model to determine the point-source magnitude of the AGN, a Sérsic profile to model the extended bulge, and a background model. As the errors reported in GALFIT only account for statistical uncertainties in the flux and are therefore frequently underestimated (C. Y. Peng et al. 2002), we adopt an iterative fitting approach to determine more accurate uncertainties. This is discussed in more detail in Appendix B.3. The final best-fit PSF magnitudes are presented in Table 2. All magnitudes reported in this table and throughout the paper are AB magnitudes.

3.3. Active Galactic Nuclei Variability

AGN are known to vary across a wide range of wavelengths, with timescales that depend on the distance from the SMBH where the emitting material is located. Higher-energy photons, such as X-rays from the hot corona, vary on timescales of days to weeks, whereas MIR emissions from warm dust vary over months to years (L. F. Sartori et al. 2018, 2019). These timescales depend on many contributing AGN properties and can differ from one source to another. Variability in the UV is primarily driven by instabilities in the accretion disk, changes in the accretion rate, and changes in the neutral hydrogen column density (N_H; e.g., M.-H. Ulrich et al. 1997; J. Dexter & E. Agol 2011; J. J. Ruan et al. 2014). Therefore, it is necessary to examine whether any differences in the point-source magnitudes measured with GALFIT using HST and Swift/UVOT data are due to the source's intrinsic variability rather than to the improved resolution of the HST data. On timescales of days to weeks, AGN variability in the UV is typically on the order of 0.05–0.2 mag, increasing to 1 mag for timescales of months to years in extreme cases (C. Ricci & B. Trakhtenbrot 2023). Large magnitude changes are usually associated with dramatic state changes or "changing-look" AGN, which are less common than the lower-magnitude variability expected from the sources in this sample (e.g., S. M. LaMassa et al. 2015; M. J. Temple et al. 2023). NGC7603 has been identified as a changing-look AGN in A. Jana et al. (2025), though no major state changes took place over the time period of these observations; it remained a Type 1 AGN, as determined by long-term monitoring of the source.

As there can be anywhere from 2 to 15 months between the Swift/UVOT and HST observations, it is necessary to determine whether any differences seen in the point-source magnitudes between the two datasets are due to the increased resolution of the HST data, excluding extended features, or if they are simply due to intrinsic variability over time.

Figure 2 shows a comparison of the differences in magnitudes derived from Swift/UVOT and HST data, obtained using both large-aperture photometry and GALFIT PSF fitting. For all but one source, the GALFIT point-source magnitude measured from HST data is smaller than that measured from Swift/UVOT data. This is not the case for the difference in magnitude measured from large-aperture photometry, which tends to be brighter when measured with HST data and generally shows smaller differences than those seen in the point-source magnitudes. The exception to this is IC 2921, the faintest source in the UV (Swift/UVOT UVM2 magnitude of 22.15), which appears brighter by ∼0.3 mag in both GALFIT point-source and large-aperture photometry using HST data. This suggests that differences in magnitude here may be driven by intrinsic variability rather than by the resolution of extended features in the HST data (which do not appear to be present in Figure 1).

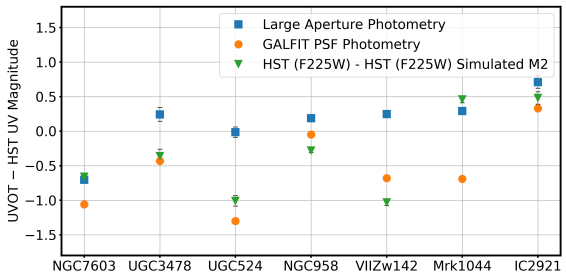

Figure 2. Magnitude differences from three different photometric measurements for each source. Blue squares: difference in the large-aperture photometry of UVM2 and F225W; orange circles: difference in the GALFIT point-source magnitude of UVM2 and F225W; green triangles: difference in the GALFIT point-source magnitude of the F225W data and the `GalSim`-simulated UVM2 data. NGC7603 compares the F225W filter with UVOT/UVW1 instead of UVOT/UVM2, as no UVM2 data were available for this source in K. K. Gupta et al. (2024). For all but one source, the difference in the point-source magnitude between HST and Swift/UVOT data is larger than that in the large-aperture photometry.

The source with the second-largest offset in UV magnitude, both in the point-source measurement and in the large-aperture photometry, is NGC 7603, which has a measured point-source magnitude in the HST F225W data that is 1.06 magnitudes fainter. However, for this source, no UVM2 data were available for the fits in G24. Therefore, for comparison, we estimated the UVM2 magnitude based on the SED of the best-fit disk model found in G24. While the lack of a direct UVM2 measurement could account for some of the differences between the derived point-source magnitude and the predicted UVM2 magnitude, a large discrepancy between the two is also expected because NGC7603 shows significant extended features in the UV imaging, which are not resolved in new UVM2 imaging, leading to contamination in the lower-resolution data. However, as previously mentioned, NGC7603 has shown high variability in the past, which may contribute to some of the differences seen here as well.

We checked for potential offsets in the point-source magnitudes caused by variability through an additional test using the Python program `GalSim` (B. Rowe et al. 2014). `GalSim` allows high-resolution images to be used to simulate how they would appear at lower resolution due to telescope or instrument effects, or to simulate the source at higher redshift. We used HST/WFC3 UVIS data to simulate how the F225W images would appear when observed with Swift/UVOT UVM2, which has approximately the same central wavelengths (2357.65 Å and 2246.43 Å, respectively). This simulation was performed by convolving a simulated Swift/UVOT UVM2 PSF with the HST F225W image and adjusting the pixel scale appropriately. Determining the point-source magnitude of this simulated image, following the same procedure as described in Section 3.2, effectively removes any potential variability, creating a new UVOT observation simultaneous with the HST data. The difference between the point-source magnitude of this simulated image and that obtained from the original HST data is shown in Figure 2. There is good agreement between the measured point-source

magnitudes when comparing HST data to both the observed and simulated Swift/UVOT data for all but one source (Mrk1044), supporting the notion that the observed differences are likely driven by the change in data quality rather than intrinsic variability for the majority of the sample.

As an additional test for the effects of variability, we constructed Swift/UVOT UVM2 light curves for all seven AGN using the available Swift monitoring data to more directly assess the role of intrinsic variability. In six of the seven sources, the peak-to-peak UV variability amplitude is smaller than the difference between the Swift/UVOT and HST F225W point-source magnitudes. NGC985, however, shows UV variability amplitudes larger than the point-source magnitude difference, with an average amplitude of about 0.3. Yet, the UVOT–HST magnitude offset is the smallest in the sample for NGC985, at 0.05 mag. These results indicate that intrinsic variability cannot account for the larger magnitude differences observed in most sources, supporting the interpretation that the offset arises primarily from differences in spatial resolution and host-galaxy contamination. For sources with small differences in the measured point-source magnitudes, intrinsic source variability may play a more significant role in the measured changes between datasets. The resulting light curves and details of their construction are discussed in more detail in Appendix C.

3.4. Spectral Energy Distribution Fitting

We now use the UV and optical point-source magnitudes from the GALFIT analysis to construct optical/UV SEDs and XSPEC-compatible PHA files for each source by converting the magnitudes to counts. No background PHA files were necessary for the fits, as the final magnitudes estimated by GALFIT were already corrected for the background in the first step of the decomposition. Response files were generated for each filter using the defined throughput in the Python package `synphot.SpectralElement` (STScI Development Team 2018).

The optical/UV region of the SED is fit in XSPEC v12.14.0, primarily using the same models as in G24. These models include the DISKPN model, a thermal accretion disk model comprising multiple blackbody components (e.g., K. Mitsuda et al. 1984; K. Makishima et al. 1986), which has been shown to successfully describe the optical/UV disk emission in many AGN sources (e.g., M. A. Malkan & W. L. W. Sargent 1982; M. A. Malkan 1983). The ZDUST model accounts for extinction due to dust grains (Y. C. Pei 1992) in the optical and UV bands, associated with the Milky Way ($\mathrm{ZDUST_{MW}}$) and the host galaxy of the AGN ($\mathrm{ZDUST_{HG}}$). The convolution model ZASHIFT shifts the disk spectrum to the redshift of the respective source. Finally, the ZTBABS model is utilized to include photoionization absorption of the AGN disk at higher energies ($\sim$0.1 keV). The final combination of models is

$$\mathrm{ZDUST_{MW}} \times \mathrm{ZDUST_{HG}} \times((\mathrm{ZTBABS}) \times \mathrm{ZASHIFT} \times \mathrm{DISKPN}). \quad (1)$$

For the two reddening components, we adopted a Milky Way (MW) extinction curve (method = 1) with $R_V = 3.08$. For dust extinction due to our Galaxy, we fixed the $E(B-V)$ values estimated by D. J. Schlegel et al. (1998) for each source. The redshifts for the two components were fixed at 0.0 for the MW and at the spectroscopically measured redshift of the source for the host-galaxy component. The inclusion of the ZTBABS model differs from the fits in G24, who did not include any photoionization absorption. To assess the inclusion of this model, we fit each source with and without it, and found that the changes in the resulting AGN properties, such as the intrinsic bolometric luminosity, remain within the expected errors. However, including this model makes the observed SED of the AGN disk more realistic by removing any significant peaks at high energies where they would not be observable. The change in the observed SED due to this model's inclusion is confined to the extreme-UV (EUV), where no HST or Swift/UVOT data currently exist, so the extent of the disk emission in this region cannot be directly measured.

For the DISKPN component, the free parameters are the maximum temperature of the disk (kT_{max}, in keV) and the host-galaxy extinction $E(B-V)$. Ideally, the normalization parameter would also be set as a free parameter; however, due to the limitation of three HST photometry points per source (compared to the 4–5 data points used in G24), we can fit only two free parameters. In contrast, G24 was able to keep the normalization free, along with the maximum disk temperature and host-galaxy dust extinction. We fix the normalization in the DISKPN model, which is defined as

$$K_{\mathrm{uvo}} = M_{\mathrm{BH}}^2 cos(i)/(D^2 \times \beta^4), \quad (2)$$

where M_{BH} is the mass of the central SMBH in solar masses, i is the inclination angle of the disk, D is the distance to the source in kiloparsec, and β is the color-to-effective temperature ratio. While using this definition to determine the normalization for a fit and fixing it, rather than leaving it as a free parameter, has been done in the past (e.g., R. V. Vasudevan & A. C. Fabian 2009), G24 presented a detailed discussion on why this approach should be applied cautiously. When using this equation, the inclination is usually assumed to be zero, and the color-to-effective temperature ratio is set to unity. G24 showed that fixing the normalization parameter can drastically affect the overall SED fitting, as the only parameter left to vary is the disk temperature. Specifically, fixing the normalization in this way causes the resulting fits to produce higher values of the X-ray bolometric correction (κ_{2-10}) by a factor of $\sim$1.3. G24 argued that using a fixed value for normalization, assuming a common inclination angle and color-to-effective temperature ratio for a large sample, is likely to severely bias the final results.

However, given the lack of a fourth data point to allow normalization to remain as a free parameter, we use Equation (1), adopting more realistic values for the color-to-effective temperature ratio rather than assuming $\beta \approx 1$, as was done in R. V. Vasudevan & A. C. Fabian (2009). Studies of narrow-line Seyfert 1 galaxies, which typically have lower accretion rates, suggest that the color temperature correction can be as high as $\sim$2.4, while S. W. Davis & S. El-Abd (2019) found an average correction factor of $\sim$1.6 by fitting synthetic spectral models for thin accretion disks.

We explore fits using fixed normalization values determined with several different correction factor values ranging from 1 (as in R. V. Vasudevan & A. C. Fabian 2009) to 2.4, to examine how this value, and therefore the normalization, affects both the quality of the fit and the resulting best-fit parameters. Larger correction factors result in the normalization being fixed to a lower value (Equation (2)), therefore

lower β values generally improve fit quality and provide more reasonable disk temperatures. This is particularly true for UGC3478 and Mrk1044, the two sources with black hole masses more than an order of magnitude lower than the rest of the sample. Their low black hole masses decrease the normalization, requiring a lower correction factor, being best fit with β values, consistent with the fits found by R. V. Vasudevan & A. C. Fabian (2009).

The X-ray data were fit also following the method of G24, using the same models and free parameters. The same binning process and the cstat statistic were applied to assess the fit quality. The model used to fit the Swift/XRT data is defined by (TBABS$_{\rm Gal}$ × ZPHABS × CABS × PEXRAV), which accounts for the primary X-ray emission, reflection from optically thick neutral circumnuclear material, Galactic absorption, and absorption by neutral material via photoelectric absorption and Compton scattering.

The UV–optical and X-rays fits were performed independently, following the fitting process in G24. Because some of the initial fits yielded larger than physically expected disk temperatures, the maximum disk temperature was limited to 0.1–10 eV, and the fit was initialized using a Gaussian prior centered on the temperature obtained in G24. Similarly, the host-galaxy extinction was initialized with a Gaussian prior based on the G24 values. The resulting best fits to both the X-ray and UV data (HST and UVOT) are shown in Figure 3. It is important to note that some of the differences in each fit may also be attributed to variability in the X-ray obscuring column density ($N_{\rm H}$), as the XRT spectrum used here corresponds to the spectrum taken closest in time to the HST UV data rather than the spectrum used in G24.

4. Results

In the previous sections, we explained in detail the steps we followed to systematically construct and fit the optical-to-X-ray SEDs of a sample of seven unobscured AGN using new, high-resolution HST data, enabling us to disentangle AGN and host-galaxy emission more fully than previously possible. In this section, we focus on the outputs of our SED fitting and compare them with those reported by G24 using Swift/UVOT data. Figure 3 show the results of our fits using HST, along with those from G24, and Table 3 lists the best-fit parameters and the integrated luminosities for each fit. The bolometric luminosity is defined as $L_{\rm X} + L_{\rm uvo}$, where $L_{\rm uvo}$ and $L_{\rm X}$ are the integrated luminosities under the best-fit model between 10^{-7}–0.1 keV and 0.1–500 keV, respectively. The bolometric luminosity of an AGN is a key diagnostic for understanding the system's physical processes, allowing determination of the Eddington ratio for each source when the SMBH mass is known.

Figure 4 shows how the bolometric luminosity derived from SED fitting with the HST data differs from the luminosity found by fitting the Swift/UVOT data in G24 for each source and as a function of SMBH mass. The difference in bolometric luminosity can be as high as 1 dex, with six of the sources showing higher values when fit to the HST data, and only one showing lower bolometric luminosity. Figure 5 shows how both the total UV/optical flux and the X-ray flux change between the two fits as a function of the change in bolometric luminosity. A clear correlation is observed between changes in the UV/optical flux and the bolometric luminosity. In contrast, no clear trend is observed when comparing these changes to variations in the X-ray flux. This highlights that the change in bolometric luminosity is driven by changes in the UV/optical fits to the HST data, rather than by changes in the X-ray contributions, which may instead be driven by intrinsic variability.

To test the correlation seen in the top panel of Figure 5, we computed the Spearman's rank correlation coefficient between Δ(UV–optical flux) and $\Delta L_{\rm bol}$, obtaining $\rho = 1.0$ for the nominal values (exact two-sided $p = 4 \times 10^{-4}$ for $n = 7$). To account for asymmetric measurement uncertainties, we performed 10,000 Monte Carlo realizations, drawing each source from its quoted error distribution. The resulting distribution of correlation coefficients has a median $\rho = 0.82^{+0.04}_{-0.11}$, with 100% of realizations yielding $\rho > 0$. The corresponding two-sided p-value for $\rho \approx 0.82$ and $n = 7$ is $p \approx 0.02$, indicating that the observed trend is unlikely to arise from random rank ordering.

As shown in Figure 3, the exact difference between the UV and optical SED is dependent on the combination of fitting parameters. The disk temperature and host-galaxy dust extinction, as well as the model normalization, which had to be left as a fixed parameter in the fits to the HST data, affect this change in different ways while also being degenerate with one another, particularly without extensive wavelength coverage in the SED data.

4.1. Disk Temperature

One of the free parameters in each fit, and one of the most thoroughly analyzed physical parameters in G24, is the maximum disk temperature. The standard accretion disk model proposed by N. I. Shakura & R. A. Sunyaev (1973) describes a geometrically thin, optically thick disk with a temperature gradient, such that higher temperatures are expected in closer proximity to the SMBH, extending up to the innermost stable circular orbit. Our SED-fitting analysis uses a multitemperature accretion disk model, allowing us to determine the maximum disk temperatures.

Figure 6 shows the difference in $kT_{\rm max}$ as a function of the change in bolometric luminosity for each source compared to the values found in G24 using Swift/UVOT data instead of HST data. While no clear correlation is present across all data points, the two sources with the largest differences in bolometric luminosity (log $L_{\rm bol}$, HST/$L_{\rm bol}$, UVOT > 1.2) show differences in maximum disk temperature greater than 5 eV. This large change in bolometric luminosity seems to be driven by this increase in the maximum disk temperature, which greatly enhances the disk emission between 0.01 and 0.1 keV, a region where no data currently exist to constrain the fits in either dataset.

The difference in derived disk temperature is most extreme for the two sources with the lowest black hole masses, UGC3478 and Mrk1044. Due to their low black hole masses, the normalization for these sources was significantly lower than that used when fitting this source in G24 (where the normalization was allowed to be a free parameter due to the larger number of available data points in the UV–optical). This discrepancy in normalization helps drive the change in disk temperature, owing to the degeneracy between these two parameters. This highlights that, even with high-resolution data, more complete SEDs spanning a wide wavelength range are needed to model AGN disks consistently and comprehensively.

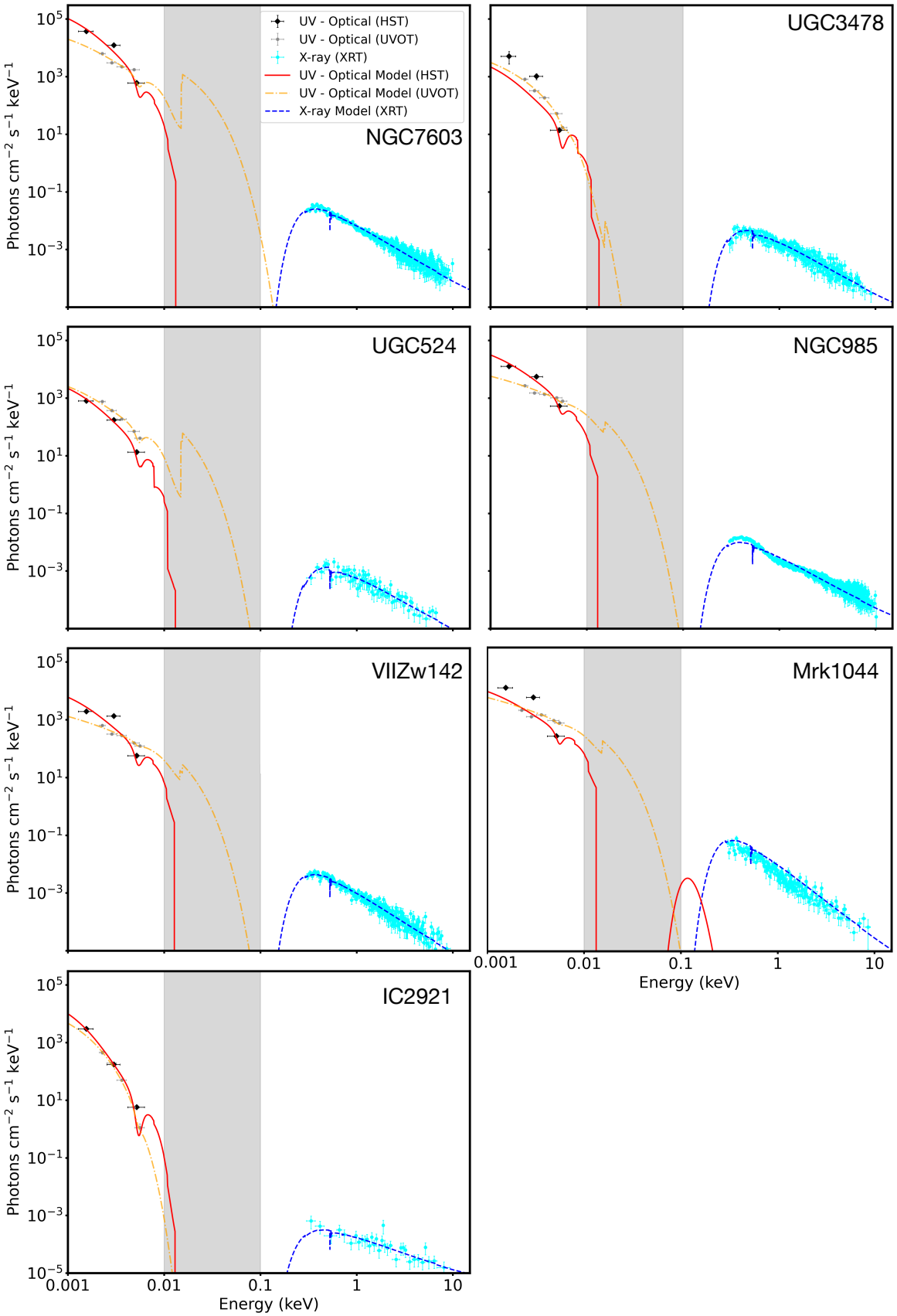

Figure 3. The optical/UV SEDs and Swift/XRT data fit with the XSPEC models as described in Section 3.4. Black data points and the red line show the HST data and fit, while gray data points and the orange line show the Swift/UVOT data and fits from G24. The models fit to the HST data include a photoionization absorption component that was not included in G24. This component affects the emission in the EUV, which is unconstrained in both datasets (shown in in gray).

Table 3
Results of XSPEC Fitting Comparing HST and Swift/UVOT

BAT ID	Counterpart Name	$kT_{\max}$	$E(B-V)$	$\log L_{\rm UV}$	$\log L_{2-10\rm keV}$	$\log L_{\rm Bol}$	$\kappa_{2-10\rm keV}$	$\alpha_{\rm ox}$
	HST/ΔG24	HST/ΔG24	HST/ΔG24	HST/ΔG24	HST/ΔG24	HST/ΔG24	HST/ΔG24	
(1)	(2)	(3)	(4)	(5)	(6)	(7)	(8)	(9)
1189	NGC7603	1.31/−4.6	0.28/0.03	45.47/0.18	43.56/−0.07	45.49/0.15	85.87/33.89	−1.50/0.02
335	UGC3478	9.98/8.9	0.59/0.48	43.95/1.08	42.30/0.01	43.99/0.73	49.29/40.92	−1.22/−0.10
34	UGC524	1.92/−1.8	0.26/−0.04	44.20/−0.20	42.80/0.09	44.26/−0.18	28.36/−25.21	−1.30/0.27
134	NGC985	2.43/−1.8	0.20/0.18	45.40/0.63	43.67/−0.08	45.43/0.45	57.67/41.12	−1.45/−0.13
9252	VIIZw142	5.81/1.9	0.34/0.29	45.56/1.05	43.33/0.18	45.57/0.96	172.7/145.1	−1.50/−0.08
130	Mrk1044	10.0/5.5	0.20/0.17	44.74/0.86	42.82/0.39	44.79/0.75	92.62/57.28	−1.23/0.25
549	IC 2921	3.87/3.3	0.86/0.67	45.39/1.35	42.87/0.05	45.40/1.11	336.2/307.7	−1.81/−0.67

Note. Column (1): Swift-BAT ID. Column (2): counterpart name. Column (3): maximum disk temperature of the best-fit model (eV) using HST. Column (4): dust extinction from the best-fit model (mag). Column (5): logarithm of the UV luminosity (erg s^{-1}). Column (6): logarithm of the X-ray luminosity (erg s^{-1}). Column (7): logarithm of the bolometric luminosity ($L_{\rm bol} = L_{\rm X} - {\rm ray} + L_{\rm uvo}$). Column (8): X-ray bolometric correction $\kappa_{2-10\rm keV} = L_{\rm bol}/L_{2-10\rm keV}$. Column (9): $\alpha_{\rm OX}$ determined from $L_{2\rm keV}$ and L_{2500}. The second value in each column is the difference between the best-fit value found in this work and that found in G24 using the Swift/UVOT data.

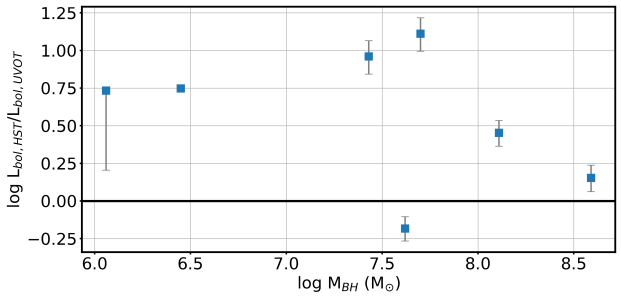

Figure 4. Ratio of the bolometric luminosity derived from the best-fit SEDs in this work using HST data in the UV–optical to the bolometric luminosity from G24 using Swift/UVOT data.

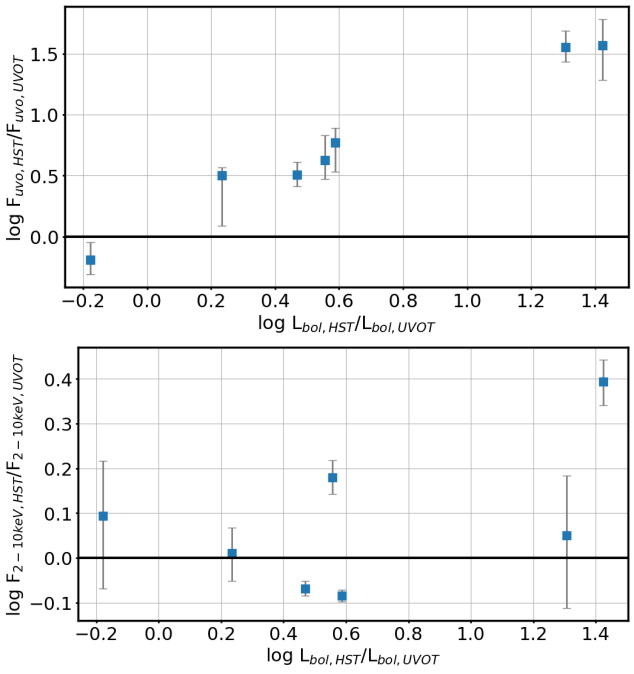

Figure 5. Top: ratio of the flux of the UV/optical disk flux (1×10^{-7}–0.1 keV) derived from the best-fit SEDs in this work using HST data to the best UV/optical flux from G24 as a function of the difference in bolometric luminosities. Bottom: same as the top, but comparing the 2–10 keV flux derived in this work to that from G24.

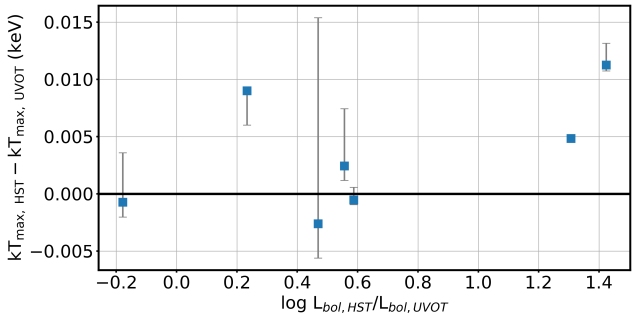

Figure 6. Difference in maximum disk temperature derived from the best-fit SEDs in this work using HST UV–optical data, compared to the maximum disk temperature from G24 using Swift/UVOT data, shown as a function of the ratio of bolometric luminosities between the two datasets.

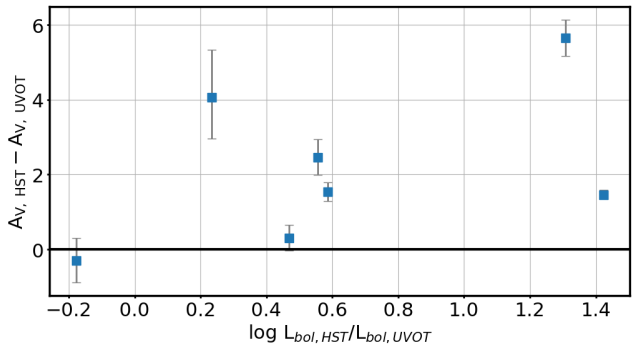

Figure 7. Difference in the extinction magnitude derived from the best-fit SEDs in this work using HST UV–optical data, compared to the extinction magnitude from G24 using Swift/UVOT data, shown as a function of the ratio of bolometric luminosities between the two datasets.

4.2. Host-galaxy Dust Extinction

One component (ZDUST) of the UV–optical SED model accounts for the intrinsic dust extinction of the source's emission due to the host galaxy, quantified by the parameter $E(B-V)$. The resulting host-galaxy dust extinction for each fit is listed in Table 3, and a comparison of the best-fit extinction with that found in G24 using the Swift/UVOT data is shown in Figure 7. For clarity, the extinction is expressed in magnitudes (A_V) in Figure 7 rather than $E(B-V)$. This

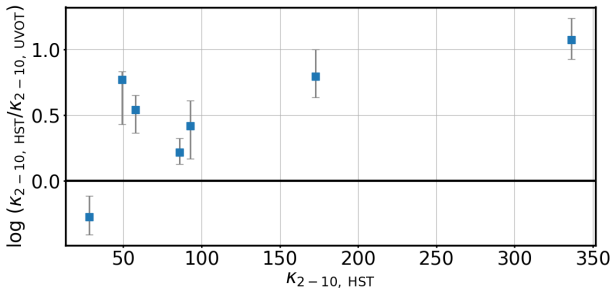

Figure 8. Difference in bolometric correction (HST – UVOT) from the best-fit SEDs of the two datasets (HST analyzed in this work and Swift/UVOT analyzed in G24), shown as a function of the bolometric correction derived from the HST data.

conversion was performed by assuming extinction properties similar to those of the SMC, as in G. T. Richards et al. (2003) and P. F. Hopkins et al. (2004).

Unlike the maximum disk temperature, the extinction magnitude derived from the HST data is larger than that found with the Swift/UVOT data for all but one source, with a maximum difference of 5.6 mag for IC 2921. It is interesting to note that, for the SEDs shown in Figure 3, NGC7603 exhibits one of the largest differences in UV emission between the HST and Swift/UVOT data (as also seen in Figure 2), but only shows a small change in the host-galaxy extinction ($\sim$0.3 mag). This highlights that the HST F225W wavelength does not probe the UV region where the greatest change in emission due to dust extinction occurs, emphasizing the need for further EUV data to properly measure the extent of UV extinction. It is also evident that the two sources with the largest change in bolometric luminosity show the largest increase in extinction. This underscores the importance of contributions to the bolometric luminosity from the EUV, as well as the NIR, where significant differences in the slope of the SED are apparent due to the constraints added by the inclusion of the HST F814W data point.

4.3. X-Ray to Bolometric Correction

Finally, we examine how the change from Swift/UVOT to higher-resolution HST data affects the bolometric correction (κ_λ). As in G24, we calculate the X-ray bolometric correction as the ratio of the bolometric luminosity ($L_{\rm bol} = L_{\rm X} + L_{\rm uvo}$) to the intrinsic X-ray luminosity ($\kappa_{2-10{\rm keV}} = L_{\rm bol}/L_{2-10{\rm keV}}$).

Figure 8 shows the change in the bolometric correction from the 2–10 keV X-ray band as a function of the value derived in this work. As expected, the extent of this change matches what is seen in Figure 4, spanning ~ -0.3 to 1.0 dex. While the exact X-ray luminosity may vary slightly due to the intrinsic variability of the source and small differences in the fits (as shown in Figure 5), both this work and G24 use Swift/XRT data, and the intrinsic X-ray luminosities do not differ significantly between the two fits. Therefore, nearly all of the change in bolometric luminosity, and consequently in the X-ray bolometric correction, is driven by differences in the UV/optical luminosity between the fits using Swift/UVOT and HST data. For two sources in our sample, we find bolometric corrections of $\kappa_{2-10{\rm keV}} > 100$. While such values are not unreasonable for sources with bolometric luminosities of log $L_{\rm bol} \approx 45.5$, as can be seen from the bolometric correction relations in works such as F. Duras et al. (2020), these sources exhibit the largest deviations in both bolometric correction and total bolometric luminosity compared to G24. This emphasizes the inherent uncertainty in measuring bolometric luminosities from limited datasets, as well as the impact of model free parameters and degeneracies on the resulting best-fit SED. To better determine AGN properties, high-resolution imaging data, such as those from HST used in this work, are required to effectively disentangle AGN and host-galaxy emission. Additionally, more complete SEDs extending into the EUV will provide vital constraints on the extent of the disk emission, helping to break the degeneracies between the model normalization and the maximum disk temperature.

5. Conclusions

In this work, we present an analysis of the resolved UV–optical SEDs for seven hard X-ray-selected AGN from the BASS survey, utilizing high-resolution HST data. We demonstrate the power of this dataset to more effectively disentangle AGN emission from that of the host galaxy than is possible with lower-resolution data, such as Swift/UVOT. Each UV–optical SED was fit with both an accretion disk model (DISKPN) and an extinction model (ZDUST) in XSPEC, following the methodology used in previous studies with Swift/UVOT data (K. K. Gupta et al. 2024).

We directly compared the HST-fitting results with those reported for G24 and found notable differences in the best-fit models. The two free parameters in our models that can be directly compared to G24 are the maximum disk temperature ($kT_{\rm max}$) and the dust extinction of the AGN in the host galaxy ($E(B-V)$). We found that the maximum disk temperature has an average difference of 0.002 keV (maximum of 0.009 keV), while the host-galaxy extinction shows an average difference of $A_V = 2.2$ (maximum of 5.7). These differences in the best-fit models have significant impacts on additional derived properties, such as the AGN bolometric luminosity ($L_{\rm bol} = L_{\rm X} + L_{\rm uvo}$), which has an average difference of 0.57 dex (maximum of 1.2 dex), leading to an average change in the X-ray-to-bolometric correction of 0.5 dex.

While these stark differences highlight the necessity of accurately disentangling AGN emission from that of the host galaxy when modeling an AGN's intrinsic properties, they also underscore the general difficulties in modeling AGN SEDs across different datasets and assumptions. As discussed in Section 3, the UV–optical SEDs constructed in this work have only three data points, which limits the available number of parameters that can be left free in the model. In contrast, G24 fit the disk model to 4–6 data points per source, allowing the normalization to be treated as a free parameter alongside the disk temperature and host-galaxy extinction. In this work, we fix the normalization using black hole mass measurements and adopt assumptions for properties such as the inclination angle and the color-to-effective temperature ratio. While we use realistic and reasonable values for these assumptions, fixing the normalization represents a key difference in the fitting techniques between G24 and this work. The significant differences found between the derived properties, particularly the maximum disk temperature, are likely a combination of differences in AGN magnitudes and fitting techniques, as G24 highlighted, due to strong degeneracies between the normalization and disk temperature. It is also important to note that the model fit to the UV data in this work includes an additional component to account for photoionization absorption, which

was not included in G24. While it was found that the best-fit parameters do not change significantly without this model, since it primarily changes the shape of the SED in a region without observations (0.01–0.1 keV), these types of changes to the fitting process may also drive some of the observed differences. Additional high-resolution EUV data would help break these degeneracies and better constrain disk models in the 0.01–0.1 keV range, where no observations currently exist in either this work or G24.

Going forward, degeneracies in AGN SED modeling results should be carefully considered, and steps should be taken to ensure that the derived AGN properties are reported as accurately as possible. This includes using the best available data to isolate AGN emission and remove any extended features in the host galaxy's bulge, as well as simultaneously modeling X-ray and UV/optical emission to reduce the limitations imposed by fixed model parameters based on the available data.

Acknowledgments

C.A. and M.K. acknowledge support from NASA through ADAP award 80NSSC22K1126.

This work was performed in part at the Aspen Center for Physics, which is supported by National Science Foundation grant PHY-2210452. The authors thank Christine Done for useful discussions regarding this work.

NASA provided support for program 16241 through a grant from the Space Telescope Science Institute, which is operated by the Association of Universities for Research in Astronomy, Inc., under NASA contract NAS 5–26555.

We gratefully acknowledge funding from ANID: CATA BASAL FB210003 (C.R., F.E.B., E.T.), the Millennium Science Initiative AIM23-0001 (F.E.B.), and FONDECYT Regular 1241005 and 1250821 (F.E.B., E.T.).

B.T. acknowledges support from the European Research Council (ERC) under the European Union's Horizon 2020 research and innovation program (grant agreement number 950533), and by the Excellence Cluster ORIGINS which is funded by the Deutsche Forschungsgemeinschaft (DFG, German Research Foundation) under Germany's Excellence Strategy – EXC 2094 – 390783311.

K.K.G. acknowledges financial support from the Belgian Federal Science Policy Office (BELSPO) in the framework of the PRODEX Programme of the European Space Agency. This research is based on observations made with the NASA/ESA Hubble Space Telescope obtained from the Space Telescope Science Institute, which is operated by the Association of Universities for Research in Astronomy, Inc., under NASA contract NAS 5–26555. These observations are associated with programs 16241 and 17310.

A.T. acknowledges financial support from the Ban-do Ricerca Fondamentale INAF 2022 Large Grant, "Toward a holistic view of the Titans: multiband observations of $z > 6$ QSOs powered by greedy supermassive black holes."

R.S. acknowledges funding from the CAS-ANID grant No. CAS220016.

M.S. acknowledges financial support from the Italian Ministry for University and Research, through grant PNRR-M4C2-I1.1-PRIN 2022-PE9-SEAWIND: Super-Eddington Accretion: Wind, INflow and Disk – F53D23001250006 – NextGenerationEU.

K.O. acknowledges support from the Korea Astronomy and Space Science Institute under the R&D program, supervised by the Korea AeroSpace Administration, and the National Research Foundation of Korea (NRF) grant funded by the Korean government (MSIT; grant No. RS-2025-00553982).

D.B.S. gratefully acknowledges support from NSF grant 2407752.

Facilities: HST (ACS and UVIS), Swift (XRT and UVOT).

Appendix A
Swift Data

Table A1 provides observational information for the Swift data used throughout this work, including the Swift/XRT data used in the fits with the HST data, as well as the Swift/UVOT data from G24 shown in Figure 3.

Table A1
Swift Observations

BAT ID (1)	Counterpart Name (2)	Swift/XRT (3)	Swift/UVOT (4)
1189	NGC7603	49538059	35365002
335	UGC3478	80373001	80373001
34	UGC524	80867001	80867001
134	NGC985	89293001	36530005
925	VII Zw 142	81213002	81213003
130	Mrk1044	35760032	35760002
549	IC 2921	80057001	80057001

Note. Column (1): Swift/BAT ID (W. H. Baumgartner et al. 2013). Column (2): counterpart galaxy name. Column (3): observation ID of the Swift/XRT data used in the fits shown in Figure 3. Column (4): observation ID of the Swift/UVOT data used in G24 and shown in Figure 3.

Appendix B
GALFIT Quality Checks

Here, we describe the image decomposition fitting procedure performed with GALFIT in more detail, including a discussion of the quality of the PSFs used in the fits, the fit residuals, and how the errors of the resulting point-source magnitudes are estimated.

B.1. Point-spread Function

As discussed in Section 3.2, GALFIT requires a reliable PSF to determine accurate point-source magnitudes for each fit. We verified the quality of the PSFs used in the GALFIT analysis by comparing them to isolated, unsaturated stars in the same HST detector and filter configuration. Each empirical or synthetic PSF was fit with a two-dimensional Gaussian function to characterize its full width at half-maximum (FWHM) and to confirm consistency with the expected instrumental resolution. Figure B1 shows examples of these fits for the model PSF used for WFC3 UVIS F225W and the PSFs created from field stars for the ACS/WFC F435W and F814W filters. Each panel displays the radial intensity profile of the PSF, the best-fitting Gaussian model, and the corresponding residuals. The fitted Gaussian widths agree with the expected HST PSF FWHM values for these filters ($\sim$0.″07–0.″09), after accounting for the pixel scale and oversampling factors applied to the PSF models. The absence of significant asymmetries indicates that the PSFs are well centered and properly sampled.

B.2. GALFIT Residuals

Here, we discuss the quality of the resulting fits from the two-dimensional surface-brightness modeling performed with GALFIT. In Figure B2, we show the observed image, the best-fitting model, and the residual image in three filters to illustrate the quality of the fits for each source. Each panel in Figure B2 displays, from left to right, the original HST image ("Data"), the GALFIT model ("Model"), and the residual ("Data – Model") after subtraction. All images are shown on the same spatial and intensity scales to facilitate visual comparison. The residuals highlight the effectiveness of the fits and any remaining nonaxisymmetric or unresolved structures. In general, the GALFIT models reproduce the central point source well, while the extended host morphology, which was not the focus of this analysis, tends to exhibit larger residual structures.

B.3. Estimating Photometric Errors

Accurate photometric uncertainties for point sources fit with GALFIT (C. Y. Peng et al. 2002) are often underestimated, especially in the presence of non-Gaussian noise, PSF mismatch, or correlated pixel noise introduced by drizzling. To obtain more realistic magnitude uncertainties for the AGN component, we generated multiple noise realizations of the best-fit model image and refit each realization with GALFIT. The scatter in the recovered magnitudes provides an empirical estimate of the photometric uncertainty that can be propagated into subsequent SED-fitting analyses.

The procedure uses the best-fit GALFIT model image as a noise-free baseline and adds synthetic noise derived from the statistical properties of the observed HST drizzled image. This produces a set of synthetic images that emulate the expected pixel-to-pixel noise characteristics of the data while preserving the model structure of the fitted galaxy and AGN.

Each realization is refit independently using the same GALFIT configuration, and the resulting parameter distributions

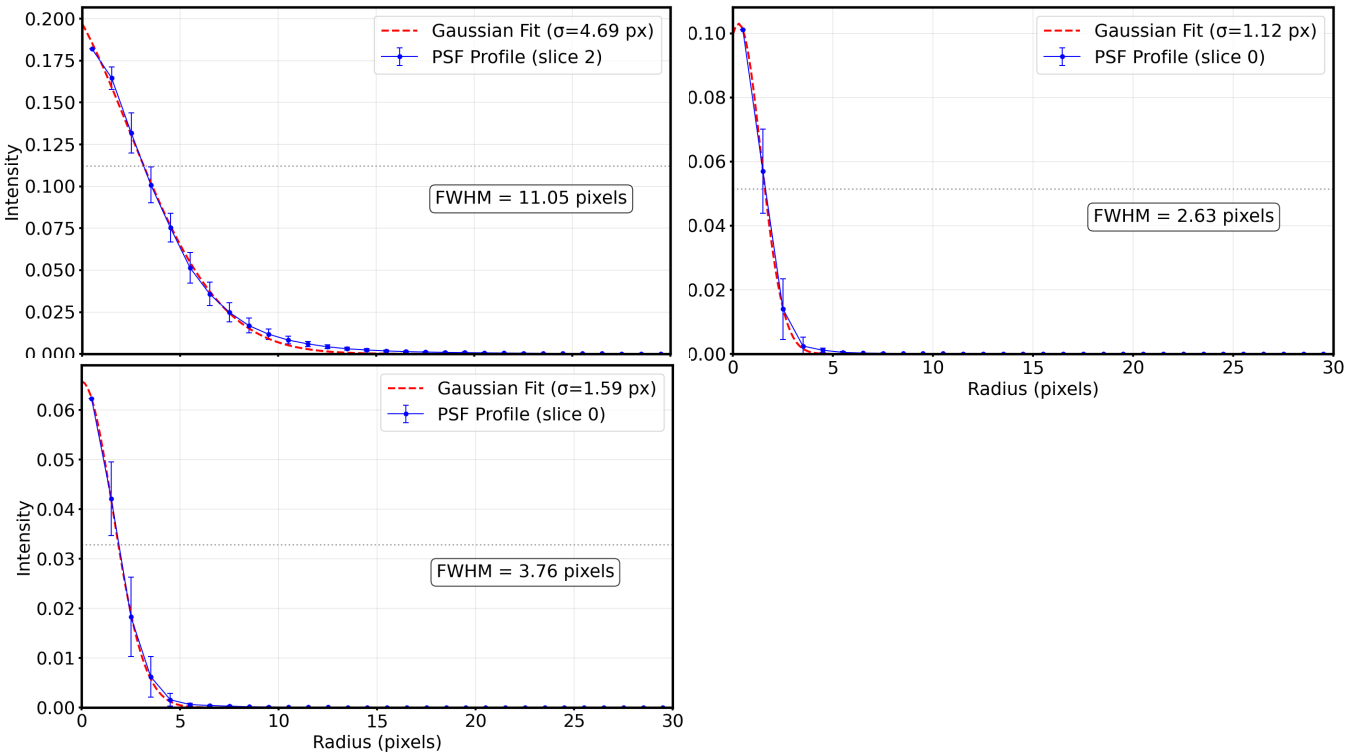

Figure B1. Example radial profiles of the model PSF used for the F225W fits (top left) and the empirical PSFs used for the F435W (top right) and F814W (bottom left) fits.

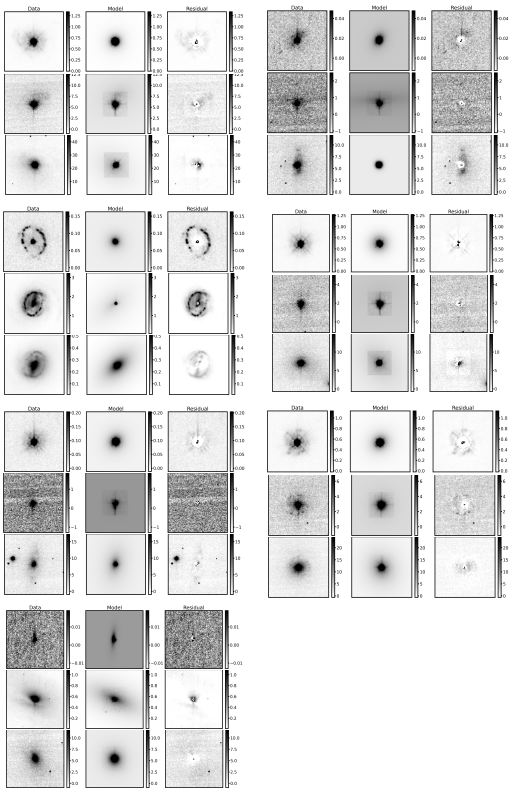

Figure B2. Results of the fits from the GALFIT analysis. Each source is grouped individually with a 3 × 3 grid showing the data, model, and residual (from left to right) for each filter. Each row shows a different filter, with F225W on the top, F435W in the middle, and F814W on the bottom. The sources are organized as follows: NGC7603 (upper left), UGC3478 (upper right), UGC524 (second left), Mrk1044 (second right), NGC985 (third left), VIIZw142 (third right), and IC 2921 (bottom left).

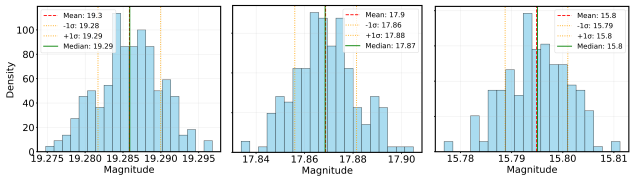

Figure B3. Results of the MCMC-GALFIT analysis used to constrain the photometric uncertainties of the best-fit point-source magnitudes for all three filters of UGC3478 (left: F225W; middle: F435W; right: F814W). This shows the point-source magnitudes from 500 realizations.

are used to estimate statistical uncertainties. This approach is conceptually similar to Markov Chain Monte Carlo (MCMC) sampling of the posterior distribution but is implemented through image-level noise perturbations. Figure B3 shows the results of this MCMC-GALFIT analysis.

Appendix C
UV Light Curves

As an additional check on the role that variability may play in driving differences in the measured point-source magnitudes between the Swift/UVOT and HST data, we construct light curves in the Swift/UVOT UVM2 filter for all seven AGN using the available Swift monitoring data. The magnitudes are

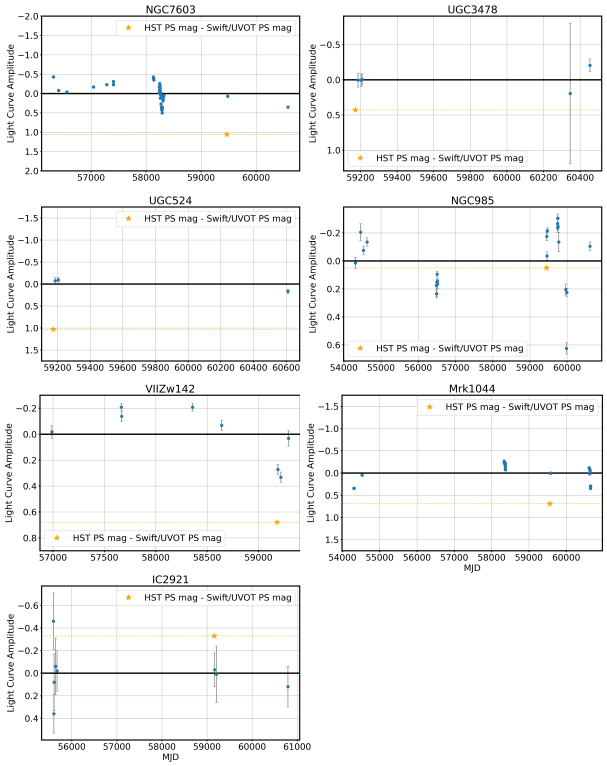

Figure C1. Swift/UVOT UVM2 light curves for the all seven BASS AGN in the sample. The light curves are constructed using large-aperture photometry with a 5″ aperture. The difference in point-source magnitude between the HST F255W and Swift/UVOT UVM2 data is shown as the yellow star. For all but two sources, NGC985 and VIIZw142, the difference in measured point-source magnitude is larger than the amplitude of the light curves.

measured following the steps outlined in the Swift/UVOT data-analysis guide, using region files for the source and background defined in SAO-DS 9. The UVM2 images were input into the `uvotsource` command from the Swift calibration database with the two region files. This is the same methodology outlined in Section 3.1 to measure the magnitudes used in the comparison of the large-aperture photometry.

Figure C1 shows the amplitude of each light curve (measured magnitude minus the mean magnitude of the entire light curve), along with the difference in the point-source magnitude measured from the HST F225W data and that measured from the Swift/UVOT UVM2 data in G24. It can be seen that, for all but one source, the light-curve amplitude is smaller than the difference in point-source magnitudes, indicating that the systematic difference between the Swift/UVOT and HST point-source magnitudes presented in Section 3 is not driven by this intrinsic variability, but is instead consistent with differences in spatial resolution and host-galaxy contamination. The source that shows variability larger than the difference in AGN point-source magnitude is also the source with the smallest difference in the measured point-source magnitude, NGC985. For this source, it cannot be ruled out that the difference in the measured point-source magnitude (0.05 mag) may be driven by variability rather than by the improved image resolution between the two datasets.

ORCID iDs

Connor Auge https://orcid.org/0000-0002-5504-8752
Michael Koss https://orcid.org/0000-0002-7998-9581
Kriti K. Gupta https://orcid.org/0009-0007-9018-1077
Claudio Ricci https://orcid.org/0000-0001-5231-2645
Benny Trakhtenbrot https://orcid.org/0000-0002-3683-7297
Franz E. Bauer https://orcid.org/0000-0002-8686-8737
Ezequiel Treister https://orcid.org/0000-0001-7568-6412
Alessandro Peca https://orcid.org/0000-0003-2196-3298
Brad Cenko https://orcid.org/0000-0003-1673-970X
Kohei Ichikawa https://orcid.org/0000-0002-4377-903X
Arghajit Jana https://orcid.org/0000-0001-7500-5752
Darshan Kakkad https://orcid.org/0000-0002-2603-2639
Richard Mushotzky https://orcid.org/0000-0002-7962-5446
Kyuseok Oh https://orcid.org/0000-0002-5037-951X
Alejandra Rojas Lilayú https://orcid.org/0000-0003-0006-8681
David Sanders https://orcid.org/0000-0002-1233-9998
Roberto Serafinelli https://orcid.org/0000-0003-1200-5071
Matilde Signorini https://orcid.org/0000-0002-8177-6905
Alessia Tortosa https://orcid.org/0000-0003-3450-6483
C. Megan Urry https://orcid.org/0000-0002-0745-9792

References

Alonso-Herrero, A., García-Burillo, S., Hönig, S. F., et al. 2021, A&A, 652, A99
Ananna, T. T., Weigel, A. K., Trakhtenbrot, B., et al. 2022, ApJS, 261, 9
Arnaud, K. A. 1996, ASPC, 101, 17
Baumgartner, W. H., Tueller, J., Markwardt, C. B., et al. 2013, ApJS, 207, 19
Berta, S., Lutz, D., Santini, P., et al. 2013, A&A, 551, A100
Boquien, M., Burgarella, D., Roehlly, Y., et al. 2019, A&A, 622, A103
Bradley, L., Sipőcz, B., Robitaille, T., et al. 2025, astropy/photutils: v2.2.0, Zenodo, doi:10.5281/zenodo.14889440
Breeveld, A. A., Curran, P. A., Hoversten, E. A., et al. 2010, MNRAS, 406, 1687
Burrows, D. N., Hill, J. E., Nousek, J. A., et al. 2005, SSRv, 120, 165
Calistro Rivera, G., Lusso, E., Hennawi, J. F., & Hogg, D. W. 2016, ApJ, 833, 98
Davis, S. W., & El-Abd, S. 2019, ApJ, 874, 23
Dexter, J., & Agol, E. 2011, ApJL, 727, L24
Duras, F., Bongiorno, A., Ricci, F., et al. 2020, A&A, 636, A73
Gehrels, N., Chincarini, G., Giommi, P., et al. 2004, ApJ, 611, 1005
Gillette, J., Koss, M. J., Kakkad, D., et al. 2026, ApJS, 282, 68
Gilli, R., Norman, C., Calura, F., et al. 2022, A&A, 666, A17
Goulding, A. D., Alexander, D. M., Bauer, F. E., et al. 2012, ApJ, 755, 5
Gupta, K. K., Ricci, C., Temple, M. J., et al. 2024, A&A, 691, A203
Hickox, R. C., & Alexander, D. M. 2018, ARA&A, 56, 625
Hill, J. E., Angelini, L., Morris, D. C., et al. 2005, SPIE, 5898, 325
Ho, L. C. 2008, ARA&A, 46, 475
Hönig, S. F. 2019, ApJ, 884, 171
Hopkins, P. F., Strauss, M. A., Hall, P. B., et al. 2004, AJ, 128, 1112
Ichikawa, K., Ricci, C., Ueda, Y., et al. 2017, ApJ, 835, 74
Ichikawa, K., Ricci, C., Ueda, Y., et al. 2019, ApJ, 870, 31
Jana, A., Ricci, C., Temple, M. J., et al. 2025, A&A, 693, A35
Kawamuro, T., Ricci, C., Mushotzky, R. F., et al. 2023, ApJS, 269, 24
Kim, M., Barth, A. J., Ho, L. C., & Son, S. 2021, ApJS, 256, 40
Kishimoto, M., Hönig, S. F., Antonucci, R., et al. 2011, A&A, 536, A78
Koss, M., Trakhtenbrot, B., Ricci, C., et al. 2017, ApJ, 850, 74
Koss, M. J., Assef, R., Baloković, M., et al. 2016, ApJ, 825, 85
Koss, M. J., Blecha, L., Bernhard, P., et al. 2018, Natur, 563, 214
Koss, M. J., Strittmatter, B., Lamperti, I., et al. 2021, ApJS, 252, 29
Koss, M. J., Trakhtenbrot, B., Ricci, C., et al. 2022a, ApJS, 261, 6
Koss, M. J., Trakhtenbrot, B., Ricci, C., et al. 2022b, ApJS, 261, 2
Koss, M. J., Trakhtenbrot, B., Ricci, C., et al. 2022c, ApJS, 261, 1
LaMassa, S. M., Cales, S., Moran, E. C., et al. 2015, ApJ, 800, 144
Lien, A. Y., Krimm, H. A., Markwardt, C. B., et al. 2025, ApJ, 989, 161
Magno, M., Smith, K. L., Wong, O. I., et al. 2025, ApJ, 981, 202
Makishima, K., Maejima, Y., Mitsuda, K., et al. 1986, ApJ, 308, 635
Malkan, M. A. 1983, ApJ, 268, 582
Malkan, M. A., & Sargent, W. L. W. 1982, ApJ, 254, 22
Martínez-Ramírez, L. N., Calistro Rivera, G., Lusso, E., et al. 2024, A&A, 688, A46
Mejía-Restrepo, J. E., Trakhtenbrot, B., Koss, M. J., et al. 2022, ApJS, 261, 5
Mitsuda, K., Inoue, H., Koyama, K., et al. 1984, PASJ, 36, 741
Netzer, H. 2015, ARA&A, 53, 365
Oh, K., Koss, M., Markwardt, C. B., et al. 2018, ApJS, 235, 4
Oh, K., Koss, M. J., Ueda, Y., et al. 2022, ApJS, 261, 4
Peca, A., Vignali, C., Gilli, R., et al. 2021, ApJ, 906, 90
Pei, Y. C. 1992, ApJ, 395, 130
Peng, C. Y., Ho, L. C., Impey, C. D., & Rix, H.-W. 2002, AJ, 124, 266
Poole, T. S., Breeveld, A. A., Page, M. J., et al. 2008, MNRAS, 383, 627
Ricci, C., & Trakhtenbrot, B. 2023, NatAs, 7, 1282
Ricci, C., Trakhtenbrot, B., Koss, M. J., et al. 2017a, Natur, 549, 488
Ricci, C., Trakhtenbrot, B., Koss, M. J., et al. 2017b, ApJS, 233, 17
Richards, G. T., Hall, P. B., Vanden Berk, D. E., et al. 2003, AJ, 126, 1131
Roming, P. W. A., Kennedy, T. E., Mason, K. O., et al. 2005, SSRv, 120, 95
Rowe, B., Jarvis, M., & Mandelbaum, R. 2014, GalSim: Modular galaxy image simulation toolkit Astrophysics Source Code Library, ascl:1402.009
Ruan, J. J., Anderson, S. F., Dexter, J., & Agol, E. 2014, ApJ, 783, 105
Sartori, L. F., Schawinski, K., Trakhtenbrot, B., et al. 2018, MNRAS, 476, L34
Sartori, L. F., Trakhtenbrot, B., Schawinski, K., et al. 2019, ApJ, 883, 139
Schlegel, D. J., Finkbeiner, D. P., & Davis, M. 1998, ApJ, 500, 525
Shakura, N. I., & Sunyaev, R. A. 1973, A&A, 24, 337
Shang, Z., Brotherton, M. S., Wills, B. J., et al. 2011, ApJS, 196, 2
Shimizu, T. T., Mushotzky, R. F., Meléndez, M., et al. 2017, MNRAS, 466, 3161
Simmons, B. D., Van Duyne, J., Urry, C. M., et al. 2011, ApJ, 734, 121
Smith, K. L., Mushotzky, R. F., Vogel, S., Shimizu, T. T., & Miller, N. 2016, ApJ, 832, 163
STScI Development Team 2018, synphot: Synthetic photometry using Astropy, Astrophysics Source Code Library, ascl:1811.001
Temple, M. J., Ricci, C., Koss, M. J., et al. 2023, MNRAS, 518, 2938
Ulrich, M.-H., Maraschi, L., & Urry, C. M. 1997, ARA&A, 35, 445
Vasudevan, R. V., & Fabian, A. C. 2009, MNRAS, 392, 1124
Vijarnwannaluk, B., Akiyama, M., Schramm, M., et al. 2024, MNRAS, 529, 3610
Yang, G., Boquien, M., Brandt, W. N., et al. 2022, ApJ, 927, 192
Yang, G., Boquien, M., Buat, V., et al. 2020, MNRAS, 491, 740